RSC Advances

RSC Publishing

PAPER

View Article Online
View Journal | View Issue

Cite this: *RSC Advances*, 2013, **3**, 5141

Single-crystal β-MnO_2 hollow bipyramids: synthesis and application in lithium ion batteries

Dan Zhan, Qinggang Zhang, Xiaohong Hu* and Tianyou Peng*

Received 10th December 2012,
Accepted 6th February 2013

DOI: 10.1039/c3ra23258a

www.rsc.org/advances

Single-crystal β-MnO_2 hollow bipyramids (HB-β-MnO_2) were synthesized *via* a template-free hydrothermal method. The as-synthesized hollow bipyramids with 100–300 nm pores along the axis direction of the β-MnO_2 bipyramids are formed through self-assembly and phase transformation processes from α-MnO_2 nanowires to β-MnO_2 bipyramids followed by chemical etching of their metastable crystal faces. Compared to the commercial bulk β-MnO_2 (c-β-MnO_2), the as-synthesized HB-β-MnO_2 exhibits a better electrochemical performance with an initial discharge capacity of 269 mA h g^{-1}, which equates to up to 0.87 Li^+ intercalation per β-MnO_2 unit, while only 0.2 Li^+ intercalation per β-MnO_2 unit is observed for the commercial c-β-MnO_2. The excellent electrochemical activity of the as-synthesized HB-β-MnO_2 can be attributed to its hollow structure and single crystal nature. The former can provide higher contact area with the electrolyte and is able to act as a buffer against volume change during the charge/discharge processes, while the latter contributes to good electronic conductivity and stable structural integrity. Moreover, the initial HB-β-MnO_2 bipyramids undergo an irreversible phase transformation to orthorhombic Li_xMnO_2 after the first discharging process, which shows good structural stability and capacity (up to 150 mA h g^{-1}) after 50 charge/discharge cycles.

Introduction

Manganese dioxide (MnO_2) as an electrode material has attracted extensive interest because of its environmental friendliness, low-cost and natural abundance. Usually, MnO_2 exists in many polymorphic forms, such as α-, β-, γ- and δ-types formed by different ways of linking its basic MnO_6 octahedral structure.[1] Among them, β-MnO_2 is constructed of single chains of edge-sharing octahedra to form 1 × 1 tunnels. Such narrow one-dimensional (1D) tunnels are difficult for Li^+ to diffuse into upon electrochemical intercalation, which makes β-MnO_2 unsuitable as an electrode material for lithium ion batteries,[2] and only 0.2 Li^+ can insert per β-MnO_2 unit, which is the equivalent to a charge storage of 61 mA h g^{-1}. On the other hand, β-MnO_2 is the most thermodynamically stable and easy to prepare, which is an important advantage for its application as an electrode material. Therefore, various approaches have been employed to improve the electrochemical activity of β-MnO_2. For instance, a β-MnO_2/C nanocomposite obtained by pyrolyzing a mixture of $Mn(NO_3)_2$ and acetylene black can electrochemically insert 1.15 Li^+ per MnO_2 unit at a cutoff voltage of 1.0 V.[3] Mesoporous β-MnO_2 is capable of reversibly accommodating Li^+ to form $Li_{0.92}MnO_2$.[4] Moreover, highly crystallized macroporous β-MnO_2 can deliver an initial discharge capacity of up to 251 mA h g^{-1}.[5]

Recently, electrode materials with three-dimensional (3D) hollow structures were found to be able to efficiently improve the electrochemical performance owing to the difference in their properties compared to the bulk form. For example, the high surface area leads to an enhanced specific capacity, the reduced effective diffusion distance causes better rate capability, and the void space in the hollow structure can buffer against the local volume change during the Li^+ insertion/deinsertion processes.[6] Therefore, MnO_2 with various hollow structures such as nanotubes,[7–9] hollow polyhedra,[10] hollow urchins,[11] and hollow cubes[12] have been synthesized. It's worth mentioning that α-MnO_2 nanotubes have been synthesized *via* a hydrothermal reaction by using $KMnO_4$ and HCl as starting materials,[13] and it was found that water molecules and K^+ ions in the precursor are inevitably introduced into the 2 × 2 tunnels of α-MnO_2 as stabilizers, which will influence the intercalation of Li^+ when α-MnO_2 is used as the electrode material for lithium ion batteries.

Herein, single-crystal β-MnO_2 hollow bipyramids (HB-β-MnO_2) were synthesized *via* a mild hydrothermal reaction using $KMnO_4$ and HCl solutions as the starting materials, which requires no templates, catalysts or surfactants as well as special post treatment for purification. A possible growth mechanism of β-MnO_2 hollow bipyramids was proposed, which is speculated to include self-assembly, dissolution/recrystallization and chemical etching processes.

College of Chemistry and Molecular Science, Wuhan University, Wuhan 430072, China. E-mail: typeng@whu.edu.cn; xhhu88@126.com; Fax: +86-27-6875-2237; Tel: +86-27-6875-2237

Furthermore, the electrochemical activity of the obtained single crystal HB-β-MnO_2 as an electrode material for lithium ion batteries was also explored. It was found that the as-synthesized single crystal HB-β-MnO_2 exhibited outstanding electrochemical activity with an initial discharge capacity as high as 269 mA h g^{-1}, which is the equivalent of up to 0.87 Li^+ intercalation per β-MnO_2 unit, while only 0.2 Li^+ intercalation per β-MnO_2 unit is achieved for the commercial bulk β-MnO_2 (c-β-MnO_2). The origin of the stark difference in electrochemical activity between the HB-β-MnO_2 and the c-β-MnO_2 was investigated in detail.

Experimental

Synthesis

All reagents were of analytical grade and used without further treatment. Deionized water was used throughout. Single-crystal β-MnO_2 hollow bipyramids (HB-β-MnO_2) were synthesized *via* a hydrothermal process based on the previous report.[13] Typically, 1.01 g $KMnO_4$ and 9.0 ml concentrated HCl (37%) solutions were added to 140 ml water with stirring to form the precursor solution. The obtained solution was transferred into a Teflon-lined stainless steel autoclave with a capacity of 200 ml. The autoclave was kept in an oven at 160 °C for 16 h, and then cooled down to room temperature. The black precipitate was collected, rinsed several times with water and absolute ethanol, and then dried at 70 °C in air overnight to obtain the product.

Material characterization and electrochemical measurements

The phase identification and structure analysis of the sample were carried out by using a Bruker D8 advance X-ray diffractometer (XRD) with Cu-Kα radiation (λ = 0.15418 nm). An overview of the morphologies and sizes of the sample was obtained on a JSM 6700F field emission scanning electron microscope (FESEM) equipped with energy-dispersive X-ray spectroscopy (EDX). TEM images and selected area electron diffraction (SAED) patterns were recorded on a JEOL JEM-2010 transmission electron microscope (TEM).

The electrochemical measurement was performed by using CR2016 coin-type cells assembled in an argon-filled glove box (Mikrouna Super 1220/750) with lithium metal as the negative electrode. The electrode was fabricated by roll-pressing a mixed paste of the active material, carbon black and PTFE with a weight ratio of 80 : 15 : 5 into a *ca.* 0.1 mm thick film and then pressing the electrode film onto a stainless mesh. The electrolyte was 1.0 M $LiPF_6$ dissolved in EC/DMC (1 : 1 in volume). A Celgard 2300 microporous membrane was used as the separator. The charge–discharge cycles were performed at different current rates between 1.5 V and 3.8 V *vs.* Li^+/Li at room temperature on a battery tester (LAND, CT2001A, China). CV data was recorded using a CHI 618C electrochemical workstation (CHI Inc., USA). All the above tests were performed at room temperature.

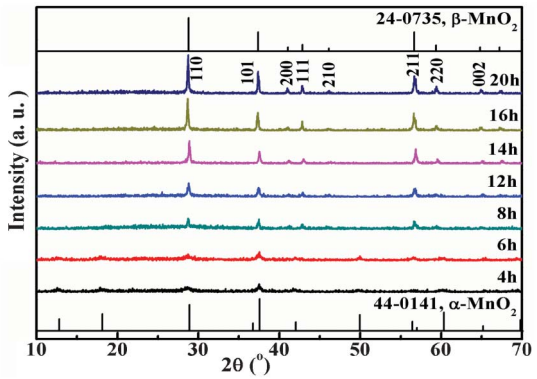

Fig. 1 XRD patterns of the products derived from different hydrothermal reaction times at 160 °C.

Results and discussion

Crystal phase and microstructure analyses

The XRD patterns of the products derived from different hydrothermal reaction times at 160 °C are shown in Fig. 1. As can be seen, the product transforms into pure β-MnO_2 with highly crystallinity after 16 h hydrothermal treatment. All the diffraction peaks at 2θ = 28.7, 37.4, 41, 42.8, 46.2, 56.7, 59.4, and 64.8° can be attributed to (110), (101), (200), (111), (210), (211), (220), and (002) planes of the β-MnO_2 with a space group of $P4_2/mnm$ (JCPDS No. 24-0735). No other characteristic peak from impurities can be observed, revealing the high phase purity of the products.

Fig. 2 shows the morphology and microstructure of the β-MnO_2 derived from 16 h hydrothermal treatment at 160 °C and the commercial β-MnO_2 (c-β-MnO_2). As shown in Fig. 2a, most of the particles show prism-like shapes with hollow interiors. The magnified images corresponding to the rectangular region (Fig. 2c) and an individual particle (Fig. 2d) show that the hollow prism possesses approximately tetragonal pyramidal ends with pores along its axial direction, which can be considered as hollow bipyramids, and therefore was

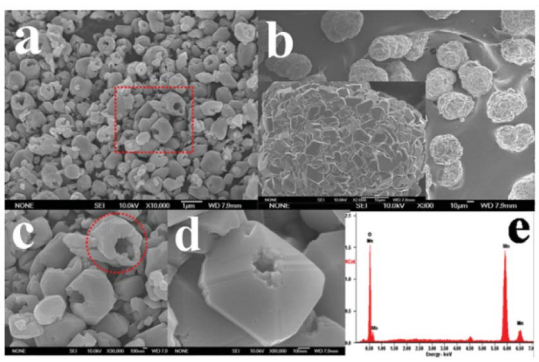

Fig. 2 SEM images of the as-synthesized β-MnO_2 (a); the commercial c-β-MnO_2 (b), the inset is a high-magnification image of a particle; the magnified view (c) corresponding to the rectangular region in (a); an individual HB-β-MnO_2 particle (d), and EDX spectrum (e) of the as-synthesized β-MnO_2.

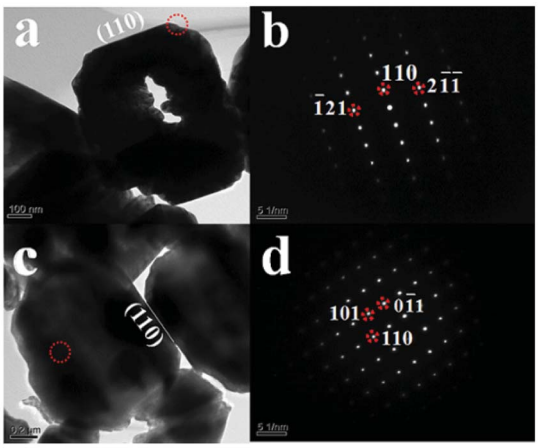

Fig. 3 TEM images (a, c) of the as-synthesized HB-β-MnO_2 in different directions; SAED pattern (b) corresponding to the circular region in (a) recorded with the axis zone [$1\bar{1}3$]; SAED pattern (d) corresponding to the circular region in (c) recorded with axis zone [$\bar{1}11$].

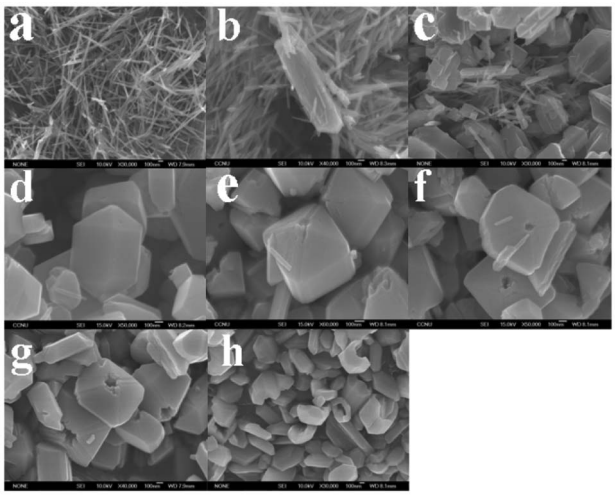

Fig. 4 SEM images of the products obtained at 160 °C for different times: a) 4 h; b) 6 h; c) 8 h; d) 12 h; e) 13 h; f) 14 h; g) 16 h; h) 20 h.

denoted as β-MnO_2 hollow bipyramids (HB-β-MnO_2) in the following section. The interior cavities of the majority of the bipyramids can be clearly observed, which have interior cavity pore sizes in the range 100–300 nm. Also, some cracked hollow particles (such as the particle marked with a dotted circle in Fig. 2c) can be observed due to erosion of the concentrated HCl. In contrast, the c-β-MnO_2 consists of very obvious aggregates from random-shaped particles with much larger particle sizes as shown in Fig. 2b.

To further detect whether some cations and water were introduced into the product during the synthesis process, an EDX spectrum of HB-β-MnO_2 was obtained and is shown in Fig. 2e. As can be seen, Mn and O atoms exist in the product at an atomic ratio of around 1 : 2, indicating that the chemical composition of the product can be approximately denoted as MnO_2 and no H_2O or K^+ exists in the formed β-MnO_2. The TEM images in Fig. 3 can further demonstrate the characteristic hollow structure of the products with different directions. The well-defined spots in both corresponding SAED patterns (Fig. 3b and 3d) imply that the as-synthesized HB-β-MnO_2 is a single crystal. The diffraction spots can be indexed to the corresponding crystal planes of the tetragonal β-MnO_2 (JCPDS No. 24-0735) as shown in Fig. 3b and 3d. Moreover, it can be concluded that the exposed side faces of the hollow bipyramids are (110) crystal faces as observed from the SAED patterns in Fig. 3b and 3d.

Overview of the formation of single crystalline HB-β-MnO_2

For a complete view of the formation process of single crystalline HB-β-MnO_2, detailed time-dependent evolutions of the crystal phase and morphology after hydrothermal treatment at 160 °C were studied, and the corresponding results are shown in Fig. 1 and Fig. 4. As can be observed from Fig. 1, the product obtained from a relatively shorter hydrothermal reaction time (4 h and 6 h) is α-MnO_2. When the reaction time was extended to more than 8 h, the crystal phase converted from the α- to β-type, and the β-MnO_2 crystallinity increased with prolonging the reaction duration. Fig. 4 shows the morphology evolution of the products derived from hydrothermal treatment at 160 °C for different reaction times. In the early stages of the reaction, α-MnO_2 nanowires are formed as shown in Fig. 4a due to the anisotropic growth driven by the chemical potential under the present hydrothermal conditions.[14]

After a longer duration (6 h), it can obviously be seen that lots of α-MnO_2 nanowires assembled spontaneously into bundles (Fig. 4b), and then some irregular thick prismatic β-MnO_2 (Fig. 4c) are formed after the hydrothermal time is extended to 8 h although some aligned nanowires can still be observed. The remaining nanowires can be ascribed to α-MnO_2 although it is very difficult to distinguish the α-MnO_2 from the corresponding XRD pattern shown in Fig. 1. However, a d-spacing of 0.49 nm can be clearly seen in the HRTEM image (Fig. 5) of a nanowire selected randomly from the product corresponding to Fig. 4c, which can be indexed to be the (200) plane of α-MnO_2 (JCPDS No. 44-0141). Therefore, it can be confirmed that the remaining nanowires observed in Fig. 4c are α-MnO_2. This result implies that the phase transformation from α- to β-MnO_2 and the morphology evolution from nanowires to prisms happened at the same time.

With up to 12 h of hydrothermal treatment at 160 °C, the product shape is a regular tetragonal prism containing two

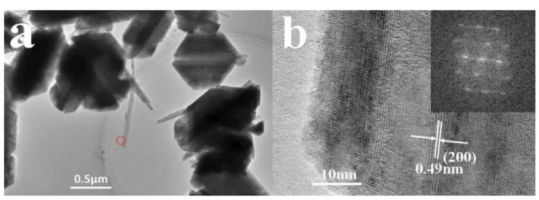

Fig. 5 TEM image (a) of the sample corresponding to Fig. 4c and the HRTEM image (b) of the selected area marked with a red circle from a nanowire in Fig. 5a.

pyramidal ends, which is similar to the tetragonal dodecahedron (Fig. 4d). The crystal phase transformation from α- to β-MnO_2 upon prolonging the hydrothermal reaction time can be attributed to the fact that β-MnO_2 is the most thermodynamically stable of all the polymorphic forms of MnO_2, and the longer hydrothermal reaction time can promote the formation of more compact β-MnO_2. Meanwhile, the primary α-MnO_2 nanowires can self-assemble into orderly bundles due to an oriented attachment mechanism[15,16] and then form larger β-MnO_2 through dissolution and re-crystallization processes. The fundamental driving force for the oriented attachment is the high surface energy resulting from the crystal defects on those α-MnO_2 nanowire surfaces, while the formation of bundles can reduce the surface-to-volume ratio, which is similar to the previous report.[15]

After 13 h and 14 h of hydrothermal treatment, the cuspate tops of the bipyramids are partly dissolved as shown in Fig. 4e and 4f. With further extension of the hydrothermal treatment time to 16 h, this section continues to dissolve gradually along the axis direction of the β-MnO_2 prism, and eventually hollow structures are produced (Fig. 4g). It has been reported that hollow α-MnO_2 nanotubes were formed by chemically etching the polar metastable surfaces of the nanorods.[13,17] In the present case, the formation of the hollow structure of β-MnO_2 seems to proceed by a similar etching process since the product was obtained under similar reaction conditions. As mentioned above, the bipyramid side faces are (110) crystal faces, which correspond to the strongest peak in the XRD pattern (Fig. 1) of the product derived from 16 h hydrothermal treatment. It means that the products are inclined to grow along the [110] orientation perpendicular to the (110) face,[18] which usually is the most stable crystal face due to the lowest surface energy in β-MnO_2. Such faces are more difficult to attack with acid solution than the end faces with higher surface energy. As a result, the end faces of the β-MnO_2 bipyramids are preferentially etched from the outside to the inside and then hollow bipyramids can be formed in order to reduce the metastable areas and enhance the lateral areas of the most stable low-index nonpolar surfaces.

The above etching process is very fast once the cracks are formed at the end of β-MnO_2 bipyramids, which can be verified by the morphology (Fig. 4h) of the product derived from 20 h hydrothermal treatment. As can be seen from Fig. 4h, those hollow bipyramids shown in Fig. 4g are almost broken, and the product is composed of crooked laminar structures with more exposed lateral areas. Note that the rough surface of the HB-β-MnO_2 as shown in Fig. 2c should be due to the corrosion caused by the coexistance of HCl. Based on the above analyses and discussion, it can be concluded that the present single crystal hollow β-MnO_2 bipyramids are formed through self-assembly and phase transformation from α-MnO_2 nanowires to β-MnO_2 bipyramids, followed by chemical etching of the metastable polar planes of β-MnO_2 bipyramids as illustrated in Fig. 6.

Electrochemical properties of single crystalline HB-β-MnO_2

To evaluate the electrochemical properties of the HB-β-MnO_2, their CV and galvanostatic charge–discharge performances were tested. Fig. 7a shows the CV curves of the HB-β-MnO_2 obtained at a scan rate of 0.2 mV s^{-1} in the potential range 1.5 to 4.3 V. The two redox peaks at 2.8 and 3.2 V can be clearly observed, suggesting the insertion/extraction of Li^+ ions in the lattice framework of HB-β-MnO_2, which agrees with the previous reports.[4] Fig. 7b shows the potential *vs.* composition curves for the first cycle of galvanostatic cycling of the HB-β-MnO_2 and c-β-MnO_2 performed at 10 mA g^{-1} in the 1.5–3.8 V potential window. As can be seen, the as-synthesized HB-β-MnO_2 delivers an initial discharge capacity as high as 269 mA h g^{-1}, which is the equivalent of up to 0.87 Li^+ intercalation per β-MnO_2 unit. In contrast, the commercial c-β-MnO_2 exhibits a much lower intercalation capacity of Li^+, which is ~0.2 Li^+ intercalation per MnO_2 unit.

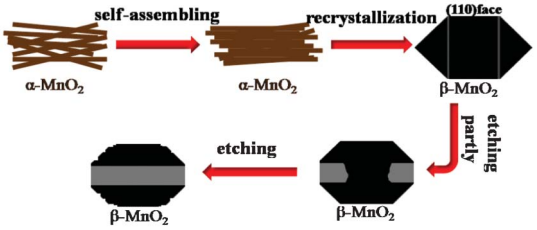

Fig. 6 Schematic illustration of the development of single crystal β-MnO_2 hollow bipyramids from a side view during the hydrothermal process.

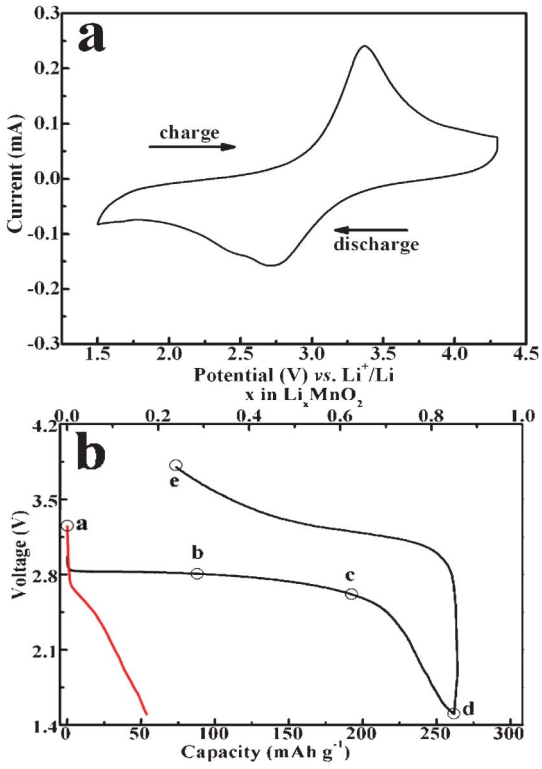

Fig. 7 a) CV curves of the HB-β-MnO_2 at a scan rate of 0.2 mV s^{-1} in the voltage range of 1.3 to 4.3 V; b) potential *vs.* composition curves for the first cycle of the galvanostatic cycling of the HB-β-MnO_2 (black lines) and c-β-MnO_2 (red line) performed at 10 mA g^{-1} in the 1.5–3.8 V potential window.

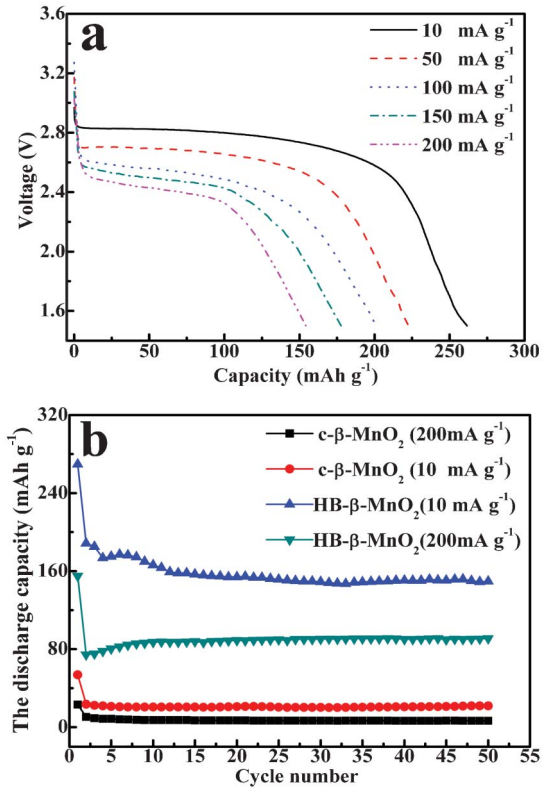

Fig. 8 a) The initial discharge curves at different current densities for the HB-β-MnO_2; b) capacity retention for the HB-β-MnO_2 and c-β-MnO_2 at 10 mA g^{-1} and 200 mAg^{-1} in the range 1.5–3.8 V.

Even at higher current densities, the HB-β-MnO_2 shows a much higher electrochemical activity than the c-β-MnO_2 at 10 mA g^{-1}. As shown in Fig. 8a, at the current rates of 10, 50, 100, 150, 200 mA g^{-1}, the HB-β-MnO_2 delivers initial discharge capacities of 269, 223, 201, 178, 154 mA h g^{-1}, respectively. The capacity decreases with enhancing current density, indicating the diffusion-controlled kinetic process for the electrode reaction.[19] The results suggest that the HB-β-MnO_2 has excellent rate capability and electronic conductivity. Fig. 8b shows the cycle performance of the HB-β-MnO_2. After the initial discharge/charge cycle, the discharge capacity of the HB-β-MnO_2 decayed significantly, which might be caused by complicated side-reactions such as irreversible structure transformation.[20] However, the HB-β-MnO_2 shows a relatively smaller capacity drop during the repeated charge/discharge process, and 150 mA h g^{-1} can still be retained after 50 charge/discharge cycles at 10 mA g^{-1}. Moreover, the as-synthesized HB-β-MnO_2 displays a similar trait of capacity drop at a high current rate of 200 mA h g^{-1}, which still retains a discharge capacity of 91 mA h g^{-1} after 50 charge/discharge cycles. Whereas, c-β-MnO_2 can only deliver an initial discharge capacity of 53 mA h g^{-1} at a current rate of 10 mA g^{-1} and 23 mA h g^{-1} at a current rate of 200 mA g^{-1}. In spite of the similar capacity drop trend with the HB-β-MnO_2, the c-β-MnO_2 retains almost no capacity after the first charge/discharge cycle especially at a high current rate of 200 mA g^{-1}. Apparently, the present HB-β-MnO_2 has a much better electrochemical activity than the c-β-MnO_2.

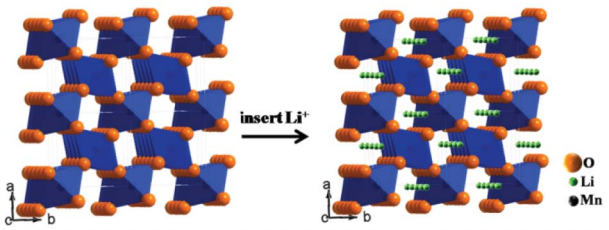

Fig. 9 Schematic illustration for the insertion process of lithium ions into the structure of β-MnO_2.

When MnO_2 is used as an electrode material for Li^+ ion batteries, the charge–discharge capacity results from Li^+ deintercalation/intercalation with the matrix, which can be formulated as in the following equation:

$$MnO_2 + xLi^+ \underset{\text{charge}}{\overset{\text{discharge}}{\rightleftharpoons}} Li_xMnO_2 \quad (1)$$

The redox process is accomplished by the intercalation of Li^+ from the electrolyte into β-MnO_2 upon discharge and the deintercalation of Li^+ from β-MnO_2 into the electrolyte upon charging as shown in Fig. 9.[21] As mentioned above, a very limited amount of Li^+ (~0.2 Li^+ per β-MnO_2) can be intercalated electrochemically into c-β-MnO_2 due to its narrow one-dimensional 1 × 1 channel.[1] However, the present HB-β-MnO_2 with hollow structures can provide more contact area with the electrolyte since the interior hollow space allows easy penetration of the electrolyte into the inner region of the electrode, and the interior hollow architecture can buffer the volume expansion/contraction caused by the Li^+ ion insertion/extraction process.[22] In addition, the single crystal nature of the present HB-β-MnO_2 has some advantages including a well-defined geometry and perfect crystallization, which can be attributed to the fine electronic conductivity and structural integrity stability.[22] Ordered atom arrangement can also facilitate fast Li^+ diffusion in the solid. As a result, the as-synthesized HB-β-MnO_2 shows an electrochemical activity superior to the commercial c-β-MnO_2.

Preliminary discussion on the Li^+ insertion/extraction mechanism of HB-β-MnO_2

It has been reported that the 1 × 1 tunnels of β-MnO_2 are less stable after Li^+ insertion, and a phase transformation may occur due to the Li^+ intercalation into β-MnO_2 during the discharge/charge process.[23,24] To investigate the structure conversion of the as-synthesized HB-β-MnO_2 along with the discharge/charge processes, galvanostatic cycling was carried out and the voltage profiles after different cycles were compared. Fig. 10 shows the discharge/charge profiles of HB-β-MnO_2 for the 1st, 2nd, 10th and 20th cycles at 10 mA g^{-1} in the range 1.5–3.8 V. A long flat plateau at ~2.8 V can be observed clearly in the 1st discharge curve, suggesting that the HB-β-MnO_2 structure as an electrode material can be main-

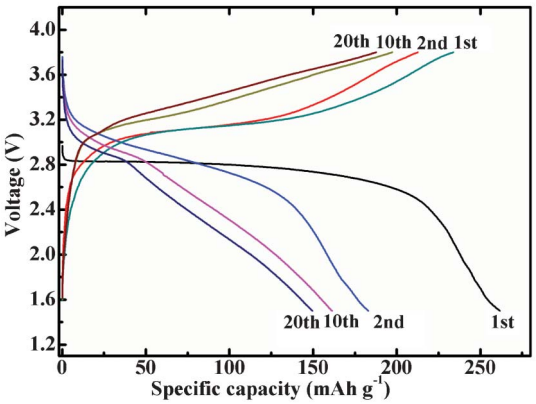

Fig. 10 Discharge/charge profiles of HB-β-MnO_2 for the 1st, 2nd, 10th and 20th cycles at 10 mA g^{-1} in the 1.5–3.8 V potential window.

tained at this point. However, the shape of the subsequent charging curves changed enormously especially after the 1st cycle, indicating that another different phase might be formed after Li^+ insertion into the HB-β-MnO_2, which then leads to the drastic decay for the 1st discharge capacity.

Since the drastic change in the charging curve of HB-β-MnO_2 occurred after the 1st discharge/charge cycle, it is necessary to further investigate the structure conversion. XRD analyses of the electrode slices were employed for different charge/discharge states for the 1st cycle as shown in Fig. 11. Each curve in Fig. 11 corresponds to the different states of the electrode marked with a, b, c, d and e in Fig. 7. Fig. 11a shows the XRD pattern of the original electrode before discharging, which is mainly indexed to β-MnO_2 (JCPDS No. 24-0735) besides the steel. Compared to the XRD pattern of the pure β-MnO_2 corresponding to Fig. 1, some burrs can be observed in this curve, which mainly result from amorphous carbon black and PTFE introduced during the electrode preparation. Upon discharging to 2.7 V, the (110) diffraction peak intensity at about $2\theta = 29^\circ$ of β-MnO_2 decreased with the appearance of a very weak peak at about $2\theta = 25^\circ$ (Fig. 11b), which is likely to correspond to the (110) peak of orthorhombic Li_xMnO_2.[23,25] It

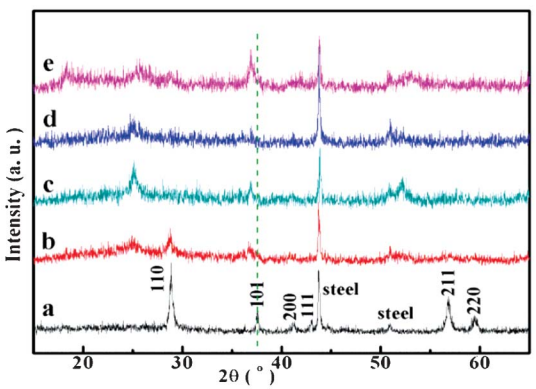

Fig. 11 XRD patterns of the β-MnO_2 electrode before cycling (a), and discharged to 2.7 V (b), 2.5 V (c), 1.5 V (d); and then charged to 3.8 V (e), which correspond to the points in Fig. 7, respectively.

indicates that a very small quantity of orthorhombic Li_xMnO_2 was formed as the Li^+ inserted into β- MnO_2. Meanwhile, the (101) peak at $2\theta = 37^\circ$ corresponding to β-MnO_2 shifts towards a lower angle, suggesting an increase in lattice spacing and expansion in lattice volume.[26]

Further Li^+ insertion into β-MnO_2 can result in gradual phase transformation. As shown in Fig. 11c, the (110) peak at $2\theta = 29^\circ$ of β-MnO_2 disappeared totally and the (110) peak at about $2\theta = 25^\circ$ of orthorhombic Li_xMnO_2 become stronger upon discharging to 2.5 V, revealing the formation of orthorhombic Li_xMnO_2. When the electrode was discharged to 1.5 V (the capacity reaches about 269 mA h g^{-1}), no obvious peak corresponding to β-MnO_2 can be observed in Fig. 11d, implying that β-MnO_2 is completely converted to orthorhombic Li_xMnO_2. At the end of the subsequent charging (to the cut-off voltage of 3.8 V) process, those diffraction peaks of β-MnO_2 are totally invisible , and another very weak diffraction peak emerged at $2\theta = 15^\circ$ as shown in Fig. 11e, which can be indexed to the (010) peak of orthorhombic Li_xMnO_2. The above results indicate that some of the Li^+ ions inserted during the 1st discharging process can not be completely lost during the following charging process, which remained as Li_xMnO_2 to stabilize the material structure and may account for the first irreversible capacity loss as shown in Fig. 8.

There are several studies on the structure variation during the electrochemical cycle by using β-MnO_2 as electrode materials. For example, Tang and co-workers thought that the electrochemical Li^+ insertion progressed topotactically for well-dispersed β-MnO_2 nanocrystals, which can retain the tetragonal framework structure.[3] From the electrochemical PXRD data, Jiao and Bruce concluded that the intercalation of Li^+ into the walls of the mesoporous β-MnO_2 occurred with minimal distortion of the structures involving two closely related phases.[4] Moreover, it has been reported that highly crystallized macroporous β-MnO_2 irreversibly transformed to an orthorhombic Li_xMnO_2 and then cycled within the new developed phase in the subsequent Li^+ insertion/extraction processes.[5] In the present situation, the original tetragonal structure of β-MnO_2 is also retained when a small quantity Li^+ ions was electrochemically inserted, and then transformed gradually to orthorhombic Li_xMnO_2 along with enhancing the Li^+ ion intercalation level. We also try to explain the stark difference in Li/Mn ratio or the first discharge capacity between the as-synthesized HB-β-MnO_2 and commercial c-β-MnO_2 from another point of view.

As an electrode material for lithium ion batteries, β-MnO_2 applies the narrow 1 × 1 tunnel parallel to the *c*-axis for Li^+ insertion/deinsertion.[1] As mentioned above, the electrochemical insertion of Li^+ ions into the 1 × 1 tunnel leads to the lattice expansion of β-MnO_2, which is inevitably accompanied by strain in the particle. In order to endure such a strain, the structure of β-MnO_2 should undergo a plastic, rather than elastic, deformation of the host lattice during Li^+ insertion/deinsertion. Sayle and co-workers[27] predicted that the β-MnO_2 host should be symmetrically porous by simulation of the insertion of Li^+ into nanostructured β-MnO_2 as a host lattice at an atomistic level. The prediction is confirmed by the application of mesoporous β-MnO_2[4] and other porous or hollow β-MnO_2.[5,26] As to the present β-MnO_2, the hollow

structure has the ability to act as a buffer against the volume expansion and maintains the primary structure of the host when Li^+ ions are inserted. Therefore, the host structure of the present HB-β-MnO_2 does not completely collapse with increasing the amount of Li^+ insertion. As a result, the present β-MnO_2 hollow bipyramids can reach a higher Li/Mn ratio than the commercial c-β-MnO_2.

Conclusions

Single-crystal β-MnO_2 hollow bipyramids with pores along the axis directions were synthesized through a template-free hydrothermal reaction by using $KMnO_4$ and HCl solutions as raw materials. The pore size of the sample was in the range 100–300 nm and shell thickness in the range 300–500 nm. It was found that the formation of β-MnO_2 with such morphology goes primarily by self-assembly and phase transformation from α-MnO_2 nanowires to β-MnO_2 bipyramids followed by a chemical etching of the metastable crystal planes of β-MnO_2. The obtained single crystal β-MnO_2 hollow bipyramids as cathode materials for lithium ion batteries exhibited an initial discharge capacity as high as 269 mA h g^{-1} at a current rate of 10 mA g^{-1}, which is the equivalent of up to 0.87 Li^+ intercalation per β-MnO_2 unit, while 0.2 Li^+ intercalation per β-MnO_2 is achieved for the commercial bulk β-MnO_2. Even at a high current rate of 200 mA g^{-1}, the initial discharge capacity can reach 154 mA h g^{-1}. Although the capacity fades drastically after the first cycle, the present β-MnO_2 hollow bipyramids show a relatively tiny drop in the subsequent electrochemical cycle, and a capacity of 150 mA h g^{-1} can still be retained after 50 charge/discharge cycles. The excellent electrochemical activity of the as-synthesized HB-β-MnO_2 can be attributed to its hollow structure and single crystal nature, which can provide a larger contact area, shorter Li^+ diffusion distance, better electronic conductivity and buffer ability against volume change during charge/discharge processes compared to the commercial bulk β-MnO_2. Considering the remarkably improved performance, the low-cost of raw materials and the synthetic operability, the present single-crystal hollow β-MnO_2 bipyramids would be promising cathode materials for high-power lithium ion batteries.

Acknowledgements

This work was supported by the Program for New Century Excellent Talents in University (NCET-07-0637), and the Fundamental Research Funds for the Central Universities (2081003) of China.

Notes and references

1 T. M. Michael, *Prog. Solid State Chem.*, 1997, **25**, 1–71.
2 J. M. L. Jungbae Lee, S. Yoon, S. Kim, J. Sohn, K. Rhee and H. Sohn, *J. Power Sources*, 2008, **183**, 325–329.
3 W. Tang, X. Yang, Z. Liu and K. Ooi, *J. Mater. Chem.*, 2003, **13**, 2989–2995.
4 F. Jiao and P. G. Bruce, *Adv. Mater.*, 2007, **19**, 657–660.
5 X. Huang, D. Lv, Q. Zhang, H. Chang, J. Gan and Y. Yang, *Electrochim. Acta*, 2010, **55**, 4915–4920.
6 X. W. Lou, L. A. Archer and Z. Yang, *Adv. Mater.*, 2008, **20**, 3987–4019.
7 L. Li, C. Nan, J. Lu, Q. Peng and Y. Li, *Chem. Commun.*, 2012, **48**, 6945–6947.
8 D. Zheng, S. Sun, W. Fan, H. Yu, C. Fan, G. Cao, Z. Yin and X. Song, *J. Phys. Chem. B*, 2005, **109**, 16439–16443.
9 W. Xiao, H. Xia, J. Y. H. Fuh and L. Lu, *J. Power Sources*, 2009, **193**, 935–938.
10 N. Chen, K. Wang, X. Zhang, X. Chang, L. Kang and Z.-H. Liu, *Colloids Surf., A*, 2011, **387**, 10–16.
11 B. Li, G. Rong, Y. Xie, L. Huang and C. Feng, *Inorg. Chem.*, 2006, **45**, 6404–6410.
12 L. Wang, F. Tang, K. Ozawa, Z.G. Chen, A. Mukherj, Y. Zhu, J. Zou, H.M. Cheng and G. Q. Lu, *Angew. Chem.*, 2009, **121**, 7182–7185.
13 J. Luo, H. T. Zhu, H. M. Fan, J. K. Liang, H. L. Shi, G. H. Rao, J. B. Li, Z. M. Du and Z. X. Shen, *J. Phys. Chem. C*, 2008, **112**, 12594–12598.
14 W. Xiao, D. Wang and X. W. Lou, *J. Phys. Chem. C*, 2010, **114**, 1694–1700.
15 X. Zhang, W. Yang, J. Yang and D. G. Evans, *J. Cryst. Growth*, 2008, **310**, 716–722.
16 E. Horváth, Á. Kukovecz, Z. Kónya and I. Kiricsi, *Chem. Mater.*, 2007, **19**, 927–931.
17 Y. Zhang, L. Chen, Z. Zheng and F. Yang, *Solid State Sci.*, 2009, **11**, 1265–1269.
18 L. Ye, L. Zan, L. Tian, T. Peng and J. Zhang, *Chem. Commun.*, 2011, **47**, 6951–6953.
19 R. Santhanam and B. Rambabu, *J. Power Sources*, 2010, **195**, 4313–4317.
20 J. H. Zeng, Y. F. Wang, Y. Yang and J. Zhang, *J. Mater. Chem.*, 2010, **20**, 10915–10918.
21 F. Cheng, J. Zhao, W. Song, C. Li, H. Ma, J. Chen and P. Shen, *Inorg. Chem.*, 2006, **45**, 2038–2044.
22 Y. L. Ding, J. A. Xie, G. S. Cao, T. J. Zhu, H. M. Yu and X. B. Zhao, *Adv. Funct. Mater.*, 2011, **21**, 348–355.
23 W. I. F. David, M. M. Thackeray, P. G. Bruce and J. B. Goodenough, *Mater. Res. Bull.*, 1984, **19**, 99–106.
24 P. Liu, S.-H. L., Y. Yan, C. E. Tracy and J. A. Turner, *J. Power Sources*, 2006, **158**, 659–662.
25 C. M. Julien and M. Massot, *Mater. Sci. Eng., B*, 2003, **100**, 69–78.
26 W.M. Chen, L. Qie, Q.G. Shao, L.X. Yuan, W.X. Zhang and Y.H. Huang, *ACS Appl. Mater. Interfaces*, 2012, **4**, 3047–3053.
27 T. X. T. Sayle, R. R. Maphanga, P. E. Ngoepe and D. C. Sayle, *J. Am. Chem. Soc.*, 2009, **131**, 6161–6173.